Molecular dynamics simulations of austenite-martensite interface migration in NiTi alloy

Gabriel Plummer, Mikhail I. Mendelev, and John W. Lawson

Phys. Rev. Materials **6**, 123601 — Published 5 December 2022

DOI: 10.1103/PhysRevMaterials.6.123601

Molecular Dynamics Simulations of Austenite-Martensite Interface Migration in NiTi Alloy

Gabriel Plummer[1],* Mikhail I. Mendelev[2],† and John W. Lawson[2]
[1] *KBR Inc., Intelligent Systems Division, NASA Ames Research Center, Moffett Field, California 94035 USA*
[2] *Intelligent Systems Division, NASA Ames Research Center, Moffett Field, California 94035 USA*

The mechanism of austenite-martensite interface migration is a key component in understanding the phase transformations in shape memory alloys. It is also intimately tied to their observed hysteresis. Molecular dynamics simulations offer a unique capability to study phase transformations in detail, however, their associated time scales prevent the observation of interface formation via nucleation and growth near the transformation temperature. To address this challenge, we present a new simulation methodology in which steady-state austenite-martensite interfaces are allowed to form close to equilibrium. The resulting structures contain well-defined interfaces which can be perturbed from equilibrium to study their migration. In NiTi specifically, the austenite-martensite interfaces are semi-coherent, made up of terrace planes separated by structural disconnections. The disconnections advance via kink pairs and provide an atomic-scale mechanism for interface migration. The methodology and results presented here provide a foundation toward further leveraging molecular dynamics simulations to better understand how the atomic-scale structure of austenite-martensite interfaces impacts macroscopic properties such as hysteresis in shape memory alloys.

I. INTRODUCTION

Shape memory alloys (SMAs), materials which undergo a reversible martensitic phase transformation induced by either temperature or stress, are the subject of intensive research due to their numerous applications in aerospace, biomedical, and other fields [1]. Among the numerous SMAs, NiTi alloys are the most studied owing to their early development, desirable mechanical properties, and near-ambient transformation temperature [2]. One of the primary characteristics of martensitic transformations in SMAs is hysteresis, due to their first order nature. This hysteresis is observed in transformations induced by either temperature or stress, although here we limit discussion to the thermal hysteresis. A large thermal hysteresis in SMAs is typically undesirable, both because it reduces the sensitivity of the transformation to temperature, and it results in less reliable behavior over many cycles [3]. NiTi alloys, with their high temperature B2 (austenite) and low temperature B19' (martensite) phases, exhibit thermal hysteresis of about 30-50 K depending on composition and processing conditions [4], placing them far from ideal SMA behavior.

Reducing the size of thermal hysteresis remains a primary goal in SMA research, which has spurred numerous investigations into its mechanistic origins. The most popular current theory of thermal hysteresis invokes the crystallographic compatibility of austenite and martensite phases using the λ_2 parameter [3, 5]. This understanding is framed in the context of classical nucleation theory, which requires an energy barrier to first be overcome before the nucleation and growth of a new phase can take place. The interfacial and strain energy introduced by a growing nucleus are of paramount importance in determining this barrier, which in turn should be directly related to the width of thermal hysteresis. When austenite and martensite phases are highly compatible, minimal interfacial and strain energies develop, leading to easy nucleation and growth. This crystallographic approach has proven to be successful in some systems, as demonstrated by the identification of SMAs with thermal hysteresis of just a few degrees and remarkable resistance to fatigue [6, 7], but the spread in values within the same system can still be quite large, indicating there are additional factors to be taken into consideration.

The theory of crystallographic compatibility looks at austenite-martensite interfaces from a high level, taking into consideration only the lattice parameters of the two phases [3]. This neglects the fine details of their structure at the atomic-scale, which could play a significant role in macroscopic properties such as thermal hysteresis. The lack of work in this area is understandable considering the challenge of observing these interfaces at the resolutions required in experiments; only a few TEM studies have imaged austenite-martensite interfaces at the atomic-scale [8–11]. In their place, computational modeling methods can provide additional insights. Unfortunately, the length and time scales required to observe the dynamic structure of these interfaces are currently beyond the capabilities of *ab initio* techniques. However, they are quite well suited to molecular dynamics (MD) simulations making use of semi-empirical interatomic potentials. Indeed, MD simulations of NiTi in particular have become a useful tool in SMA research in recent years due to the development of several new interatomic potentials [12–15]. A number of studies have been conducted investigating both the temperature- and stress-induced martensitic transformations, providing atomic-scale detail not previously available [16–19]. The major issue with all these studies, however, is that they are conducted at rates which do not allow for well-defined austenite-

* gabriel.w.plummer@nasa.gov
† mikhail.mendelev@nasa.gov

martensite interfaces to form; typical MD simulations employ temperature ramp rates on the order of 10^{12} K/s and strain rates on the order of 10^{8} s^{-1}, many orders of magnitude faster than experiments. The result is that the more physical process of nucleation and growth associated with a first order phase transformation is not allowed to happen before the system leaves the temperature or strain region within which both phases exhibit thermodynamic stability. Therefore, the transformations occur rapidly and oftentimes simultaneously throughout the entire system, critically with a lack of well-defined austenite-martensite interfaces.

With this in mind, the primary goal of the present study was to seek a new, more physically meaningful approach to studying austenite-martensite interfaces via MD simulations. This should serve as a first step to better understanding their dynamic structure at the atomic-scale and how it can affect macroscopic properties such as thermal hysteresis. Therefore, the paper is structured as follows. First, some technical details of the MD simulations and their analysis are presented. Following this, we report a series of thermodynamic calculations which provide important context for the subsequent interface simulations. The remainder of the paper is then devoted to describing steady-state austenite-martensite interfaces, their migration under a thermodynamic driving force, and characterizing their structure at the atomic-scale. The results provide several novel insights into the importance of interface structure to the martensitic transformation in NiTi.

II. SIMULATION METHODOLOGY

All MD simulations were performed within LAMMPS [20], and visualizations were made using OVITO [21], both open-source codes. To model the interatomic interactions in NiTi we selected the modified embedded atom method (MEAM) potential developed by Ko *et al.* [13]. It has become the most widely used NiTi potential due to its ability to capture both the temperature- and stress-induced martensitic transformations between the B2 and B19' phases as well as its relative computational efficiency. All MD simulations utilized a timestep of 2 fs. Accurate identification of the B2 and B19' phases is of critical importance for determining the austenite-martensite interface structure. In MD simulations this is a nontrivial task for which a robust algorithm is yet to be developed. However, the common neighbor analysis (CNA) algorithm [22] has been successfully used to identify B2 in other MD simulations making use of the MEAM potential employed here, with B19' then being identified as a structure which is neither fcc, hcp, or bcc [13, 18, 19]. While CNA is certainly not an ideal method of structural identification for this system, it is suitable for our purposes here, and we made use of it as implemented in LAMMPS with a cutoff distance of 3.62 Å.

III. THERMODYNAMIC CONSIDERATIONS

The martensitic transformation and therefore evolution of austenite-martensite interfaces in NiTi is driven by the thermodynamics of the two competing phases. Therefore, we first performed a series of free energy calculations with the employed MEAM potential. The free energies were computed in MD simulations via thermodynamic integration (TI) using the following relation:

$$F^{MD} - F^{ref} = \int_0^1 \left\langle \frac{\partial U}{\partial \lambda} \right\rangle_\lambda d\lambda \tag{1}$$

where F^{ref} is the known free energy of a reference state, and U, the system potential energy, is given by: $U = \lambda U^{ref} + (1-\lambda)U^{MD}$. The parameter λ is used to smoothly transition from the interatomic potential at $\lambda = 0$ to the reference state at $\lambda = 1$. The integral in Eq. 1 can be evaluated by running a series of equilibrium MD simulations at prescribed values of λ. While accurate, this approach can be quite computationally expensive, as equilibrium simulations must run for a large number of timesteps to allow for appropriate ensemble averaging, and a reasonable number of λ values must be selected to best approximate Eq. 1. Alternatively, non-equilibrium TI provides a more efficient calculation of free energy, while retaining an impressive degree of accuracy. This approach evaluates Eq. 1 by continuously varying λ over a single simulation. The irreversible switching process introduces a systematic error, which, if the switching time is long enough, can be eliminated by averaging the results of both the forward and reverse processes, i.e. λ undergoes the following cycle: $0 \rightarrow 1 \rightarrow 0$.

The absolute free energies of bulk B2 and B19' phases were evaluated with non-equilibrium TI, as implemented in LAMMPS by Freitas *et al* [23]. Initially the free energy of B2 was evaluated at 400 K with a switching time of 2 ns and an equilibration time of 0.1 ns at $\lambda = 0$ and 1. Shorter switching and equilibration times of 0.1 ns and 0.01 ns, respectively, produced the same result to within 0.1 meV/atom demonstrating good convergence of the calculation. Therefore, all subsequent calculations made use of these shorter run times. The reference state was an Einstein crystal, which has known free energy:

$$F^{ref} = 3Nk_BTln\left(\frac{\hbar\omega}{k_BT}\right) \tag{2}$$

where ω is the oscillator frequency of the Einstein crystal related to its spring constant as $k = m\omega^2$, with m being the atomic mass. Prior to the TI, the equilibrium lattice parameters and spring constant of the phase of interest were determined at a given temperature via an isothermal-isobaric (NPT) MD simulation of 20,000 timesteps, with ensemble averaging over the last 10,000 timesteps. As described by Freitas *et al* [23], the spring constant can be estimated from the mean-squared displacement of atoms. We found this to produce an adequate reference structure for the B2 phase, but the spring

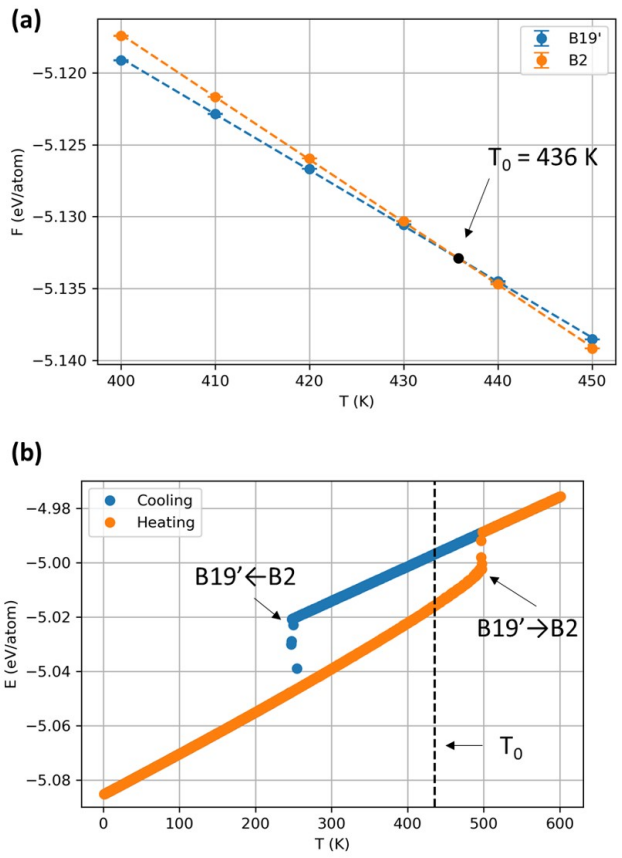

FIG. 1. (a) Bulk free energy of B2 and B19' phases calculated via non-equilibrium TI. Each data point is averaged over five independent simulations, with error bars representing the standard deviation. (b) Cooling and heating of a bulk NiTi simulation cell (16,000 atoms) demonstrating the thermal hysteresis of the martensitic phase transformation.

constant was increased by a factor of 10 for the B19' phase due to it being too soft and producing inadequate convergence of the results as a function of switching time. We note that for a reasonably chosen spring constant, the free energy of the phase under consideration does not depend on its value. As Ni and Ti are relatively similar, an Einstein crystal with a single atomic species (averaged atomic mass and spring constant) was used as the reference. All free energy calculations were performed on fully periodic simulation cells containing roughly 16,000 atoms.

Figure 1a shows the results of free energy calculations for equiatomic B2 and B19'. Linear fits of the data close to the martensitic transformation temperature (T_0) give a value of 436 K, about 80-100 K higher than typically reported experimental values for the equiatomic NiTi alloy [4, 24, 25] but in good agreement with previous *ab initio* MD simulations [26–29]. To verify the physicality of this transformation temperature, we performed a thermal cycling simulation on bulk NiTi, in which an initial cell of B2 (16,000 atoms) was cooled from 600 K to 1 K and subsequently reheated to 600 K. The simulation was performed at a rate of 0.5 K/ps within the NPT ensemble, allowing both cell volume and angles to relax simultaneously. The results from this simulation are shown in Figure 1b, which plots the potential energy of the system as a function of temperature. Upon cooling, a drop in the energy, corresponding to the transformation of B2 to B19', occurs around 250 K. Upon reheating, the B19' transforms back into B2 around 500 K. Similar results with this potential have been reported previously [13]. Importantly, T_0 falls within this thermal hysteresis, as should be the case for a first order phase transition. We note that in experiments T_0 is often estimated to be the midpoint of the hysteresis, i.e. $(A_f+M_s)/2$, but its direct calculation here shows that is not necessarily the case. The thermal hysteresis depicted in Figure 1b should not be confused with the hysteresis observed in experiments; indeed, it is an order of magnitude larger. This simply represents the metastability range of the two phases as predicted by the interatomic potential. The phase transformations correspond to the dissolution of one phase due to thermodynamic instability [30], and thus only give an upper bound for thermal hysteresis. This is a direct result of the rates employed in MD simulations, and the lack of defects in these simulation cells which preclude more physical nucleation and growth mechanisms within the metastability region.

In addition to the equiatomic NiTi alloy, we also investigated the thermodynamics of non-stoichiometric compositions. Tuning the composition of SMAs is a common method of changing properties such as transformation temperature and hysteresis; there have been a number of such studies dedicated to the NiTi alloys [4, 31, 32]. Therefore, it is instructive to test whether the current potential can capture these important effects. To accomplish this, free energy calculations were repeated on Ni_xTi_{1-x} simulation cells with $x = 0.49$ and 0.51. For each Ni concentration five independent simulation cells were created with randomized substitutional sites. We also performed hybrid Monte Carlo MD (MC/MD) simulations on these randomized structures for 100,000 timesteps to ensure no unfavorable clustering occurred, but there were no noticeable changes in the calculated free energies. Figure 2a plots the free energy differences between the B2 and B19' phases for all three compositions close to T_0, with linear fits giving different values for each composition. Figure 2b plots these T_0 values as a function of Ni concentration and compares them with the experimental results of Frenzel *et al.* [4]. The MD results exhibit the opposite trend of those from experiment, with T_0 increasing with increasing Ni concentration and decreasing with decreasing Ni concentration. This is not necessarily surprising as the potential was not explicitly developed for non-stoichiometric NiTi, but nonetheless it provides important confirmation that the potential should be confined to equiatomic NiTi. Therefore, this was the case for all subsequent MD simulations.

A final thermodynamic consideration involves surface

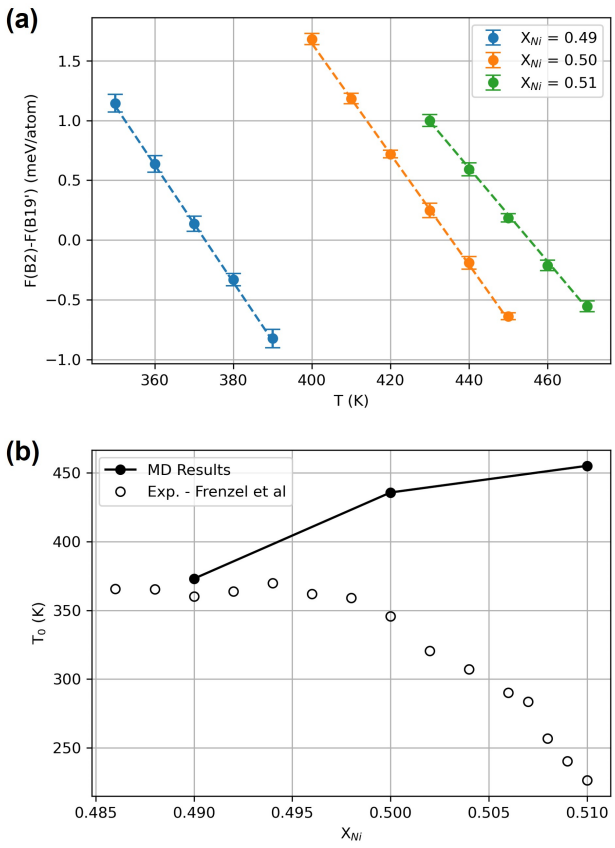

FIG. 2. (a) Bulk free energy difference of B2 and B19' phases, as calculated via non-equilibrium TI, plotted for different concentrations of Ni. Each data point is averaged over five independent simulations, with error bars representing the standard deviation. (b) Transition temperatures determined from free energy calculations compared with experimental results from various NiTi compositions. Experimental data courtesy Ref. [4].

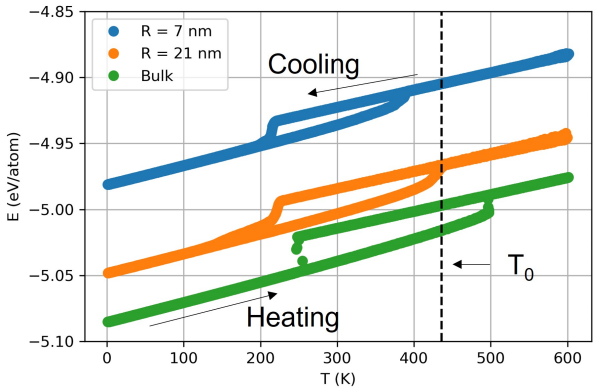

FIG. 3. Cooling and heating of spherical NiTi nanoparticles, demonstrating the dependence of thermal hysteresis on surfaces, and hence particle size. The bulk data from Figure 1b is reproduced for comparison. The bulk transformation temperature (T_0), which falls outside the hysteresis loops, is indicated by a dotted line.

effects. During a phase transformation, a growing nucleus will produce stresses in the matrix phase immediately surrounding it. On the length scales of MD simulations, these stresses are likely to extend across periodic boundaries, producing undesired effects on the growth process being studied. To remove this simulation artifact, we made use of a spherical nanoparticle geometry. While this allows for relaxation of stresses, the surfaces are expected to contribute to the thermodynamics of the two competing phases and must be accounted for. As an example, Figure 3 shows the thermal cycling results for spherical NiTi nanoparticles of two different sizes compared to the bulk results shown in Figure 1b. For the nanoparticles there is a noticeable decrease in the temperatures at which the phase transformations occur; this effect is more pronounced in the smaller nanoparticle. This is a general trend and was reported in detail by Ko *et al.* in a wide range of nanoparticle sizes; it was mainly attributed to the B2 surface energy being lower than that of B19' [19]. The effect is strong enough that the bulk value of T_0 falls outside the hysteresis loops of the nanoparticles investigated here. This indicates that T_0 in the nanoparticles is reduced from its bulk value due to surface contributions to the free energy. In subsequent simulations of austenite-martensite interfaces, the larger nanoparticle ($R = 21$ nm) was used, and its hysteresis loop in Figure 3 was an important consideration in selecting appropriate temperatures to ensure the phases are close to being in equilibrium with one another.

IV. AUSTENITE-MARTENSITE INTERFACES

To overcome the effects of enormously high MD simulation rates in studying austenite-martensite interfaces, we introduce a new methodology to allow for their natural formation close to equilibrium. This process is illustrated in Figure 4. First, we started with a spherical ($R = 21$ nm) B19' nanoparticle equilibrated at a temperature within the hysteresis loop depicted in Figure 3. Small amounts of austenite formed near the surfaces, but they did not affect subsequent steps (Figure 4a). Next, spring forces were applied to a spherical core of atoms in the center of the nanoparticle. It was then heated to a temperature outside the hysteresis loop, thus triggering transformation to B2. The purpose of the spring forces is to act as anchors, locking in the B19' nucleus when it would otherwise transform to B2. The result is a core-shell nanoparticle with a spherical B19' nucleus being completely surrounded by B2 (Figure 4b). We used a radius of 10 nm for the B19' core; smaller cores tended to dissolve once the spring forces were removed. With the spring forces still applied to the core, the nanoparticle was cooled to a temperature back inside the hys-

teresis loop, where both phases should be able to coexist at least for some time. At this point, the austenite-martensite interfaces within the core-shell nanoparticle are artificially maintained by the spring forces, and the spherical symmetry ensures that no particular crystallographic orientation is favored. Finally, to allow the interfaces to develop naturally, the spring forces were removed from the B19' core, and we applied constant energy (NVE) equilibration to the entire nanoparticle for 2 ns. This approach, which was originally developed for MD simulations of solid-liquid interfaces [33, 34], allows the two phases to come into equilibrium with one another, with the system temperature self-regulating as a result. In contrast, other attempts to equilibrate the two phases with isothermal (NVT) simulations never resulted in the formation of well-defined interfaces, as the applied temperature would force the transformation to proceed rapidly in either one direction or the other. The result of the NVE equilibration was that the initially spherical B19' core adopted a plate morphology, extending across the entirety of the nanoparticle with two well-defined, flat austenite-martensite interfaces (Figure 4c, see also Movie S1 [35]). This result is consistent with experimental observations of growing martensite and also underscores the anisotropic nature of the process, with certain interfaces evidently being more energetically favorable. Further characterization of these interfaces at the atomic-scale is the subject of later discussion. The NVE equilibration also provides an effective T_0 for the nanoparticle system as the two phases come into equilibrium with one another. After some initial fluctuation, the temperature settled in the range 420-425 K. We note that this is 10-15 K below the bulk value of T_0, and falls right on the edge of the nanoparticle hysteresis loop in Figure 3.

A. Interface Migration

The formation of well-defined austenite-martensite interfaces provides an opportunity unique to MD simulations to study their migration and the associated mechanisms at the atomic-scale. We achieved this by switching to an NVT simulation with the thermostat temperature slightly different from the equilibrium temperature determined from the NVE equilibration. The NVT simulation was run for 1 ns at the new temperature, and the interface migrated due to the newly introduced thermodynamic driving force. An example of the interface migration at 415 K is depicted in Figure 4d (see also Movie S2 [35]); notably the interfaces remain flat and well-defined as the B19' plate grows, an important feature not present in previous rate-dependent MD simulations [18, 19]. These same growth characteristics were consistent over the entire temperature range studied. The flat interfaces allow for easy measurement of the plate thickness as it grows over time (Figure 5a), which also enables determination of the austenite-martensite interface velocity (Figure 5b).

TABLE I. Steady-state interface velocities as determined from the data points in Figure 5b between 0.6 and 1.0 ns.

T (K)	v (m/s)
410	8.2 ± 0.2
415	4.6 ± 0.2
420	0.5 ± 0.1

Interface velocities were calculated by taking single slope measurements at the endpoints in Figure 5a and averaged slope measurements at interior points. At each temperature investigated, the interfaces exhibit the same qualitative behavior: an initial period lasting about 0.4 ns where the interfaces migrate at a faster rate followed by a steady-state regime where interface migration slows. The initial fast period is a transient associated with the switch from NVE to NVT ensembles, so we only consider the steady-state velocities to make comparisons. As the nanoparticle is moved further away from equilibrium, the B19' plate grows at a faster rate due to the larger thermodynamic driving force. Table I provides the steady-state interface velocities for each temperature studied. With each additional 5 K decrease of the temperature, the interface velocity increases by about 4 m/s. Additional decreases in temperature below 410 K did not allow a steady-state to be achieved prior to the entire nanoparticle transforming due to its limited size. It is notable that the interface velocity measurements made here, especially those closer to T_0, are of an order of magnitude which is observable on the time scales of experiments. In previous rate-dependent MD simulations, including the thermal cycling simulations presented here, transformations happen over the course of just a few picoseconds, which would suggest velocities approaching sonic speeds. Our results here are in much better alignment with the capability of *in situ* TEM experiments to observe the progressive martensitic transformation due to nucleation and growth [36, 37]. We also note that NVT simulation of the nanoparticle at 425 K resulted in preferential growth of the B2 matrix (Figure S1 [35]), consistent with the effective T_0 determined from the NVE equilibration.

Despite the more physical nature of the martensitic transformation observed in the preceding MD simulations, they do not allow for a direct measurement of thermal hysteresis. The reason for this is the geometry of the system, which differs in important ways from nucleation and growth in a bulk NiTi sample. The growing B19' plate in the nanoparticle does not require the formation of additional interfacial area as would be the case for a growing nucleus in the bulk. Additionally, due to the free surface of the nanoparticle there is little to no accumulation of stress in the B2 matrix. This means that growth or dissolution of the B19' plate simply occurs as a function of the bulk thermodynamics (with some surface contributions) of the competing phases, i.e. thermal hysteresis is zero. In contrast, we can use the same nanoparticle simulation cell but with a different starting

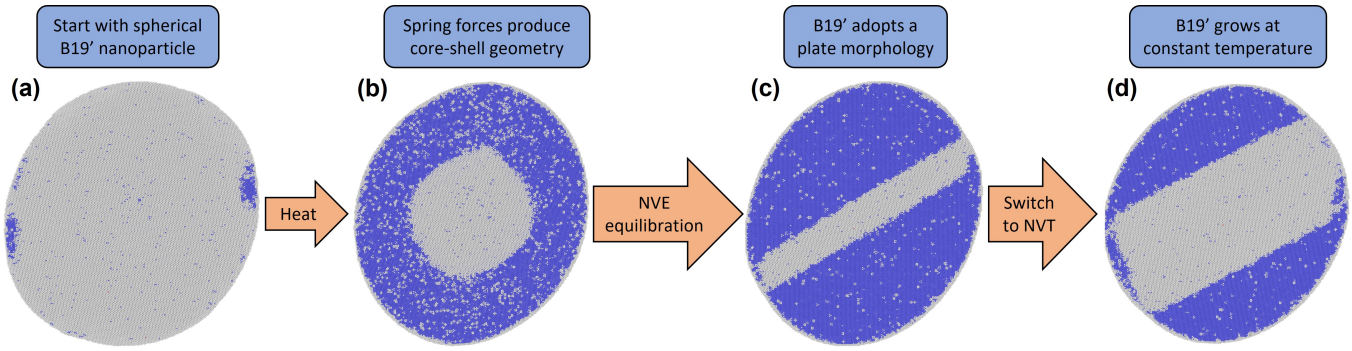

FIG. 4. Schematic depicting the MD simulation setup for creation of austenite-martensite interfaces as well as its perturbation from equilibrium to drive interface migration. Snapshots show a cross-sectional view of the center of the spherical NiTi nanoparticle. Atoms are colored according to CNA: B2 - blue, other - gray.

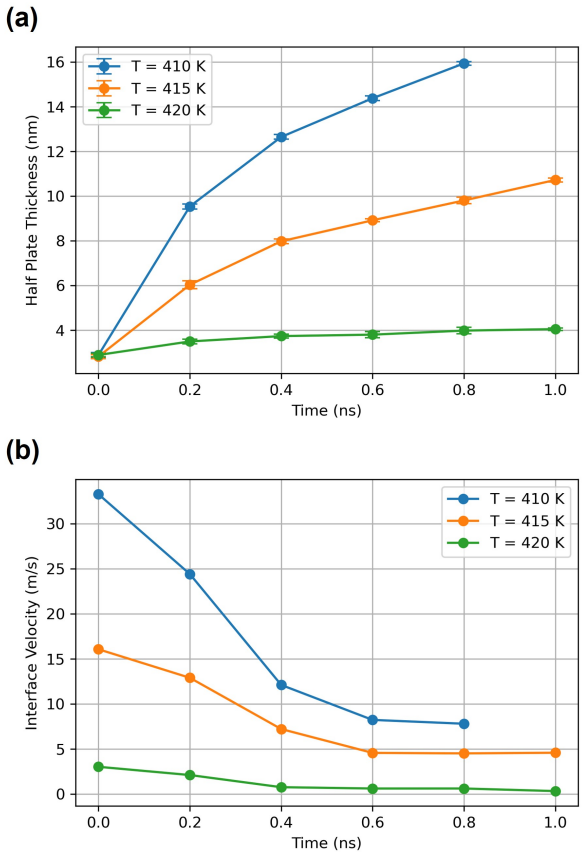

FIG. 5. (a) Growth of the B19' plate during NVT MD simulations. (b) Austenite-martensite interface velocities determined from plate thickness values in (a). The data point at 1 ns for 410 K has been omitted because the nanoparticle completely transformed prior to this.

geometry to illustrate the important role the austenite-martensite interface plays in determining thermal hysteresis. Rather than starting with a spherical B19' core, we applied spring forces to a spherical cap at one end of the nanoparticle. After undergoing the same NVE equilibration procedure described previously, the result was a B19' nucleus at the surface of the nanoparticle having the same well-defined, flat austenite-martensite interface as was the case for the B19' plate (Figure 6a). In this case, the B19' nucleus must increase the interfacial area in order to grow. As a result, it would be expected that an additional thermodynamic driving force would be required to overcome this energy barrier which was not present in the case of the B19' plate. We confirmed this by running NVT simulations for 1 ns at various temperatures. In the case of the B19' plate, growth occurred at all temperatures below 425 K. However, for this new geometry growth only occurred at temperatures below 405 K (Figure S2 [35]). We also simulated the opposite scenario, a B2 nucleus at the nanoparticle surface (Figure 6b). For this case, growth only occurred at temperatures above 425 K (Figure S2 [35]). Therefore, for this model system, we can estimate a thermal hysteresis of about 20 K solely due to the interfacial energy associated with the austenite-martensite interface. While this highly idealized setup still has significant differences from nucleation and growth in bulk NiTi, the more physical depiction of thermal hysteresis is in reasonable agreement with experiments and emphasizes the important role of the austenite-martensite interfaces in the process.

B. Interface Structure

We now focus on the atomic-scale structures of the austenite-martensite interfaces present in the nanoparticle simulations and how they impact mobility. The simulation snapshots depicted in Figures 4 and 6 were taken from single timesteps and therefore contain significant noise due to thermal vibrations of the atoms. This is apparent when inspecting the B2 phase, which has a number of atoms scattered throughout not identified as B2. Consequently, identifying the fine details of the interface structure becomes a near-impossible task. To circumvent this challenge, we use simulation snapshots with atomic positions averaged over 1,000 timesteps (at the ve-

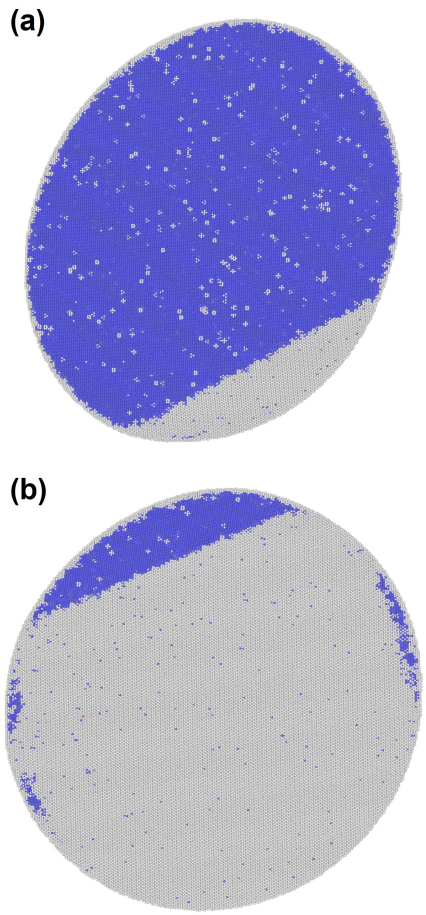

FIG. 6. (a) Snapshot of the NiTi nanoparticle after NVE equilibration with a B19' nucleus shaped as a spherical cap. (b) Snapshot of the same nanoparticle after the B19' nucleus has grown - alternatively this can be viewed as the starting state for a B2 nucleus. Atoms are colored according to CNA: B2 - blue, other - gray.

locities depicted in Table I this corresponds to interface migration of less than 0.2 Å). An example is depicted in Figure 7a, which was taken from the NVT simulation of the growing B19' plate at 415 K after 0.4 ns. The average atomic positions provide a much clearer picture of the interface structure, showing that it is made up of a regular array of steps, also known as structural disconnections [38, 39]. An additional interface, which formed with retained austenite near the nanoparticle surfaces, also becomes clear. Magnified snapshots of the two interfaces in Figures 7b and c clearly show a series of coherent terrace planes separated from one another by disconnections. Interfaces with this structure are ubiquitous in the study of solid-solid phase transformations [40], but comparatively less attention has been given to them in SMAs and how they may impact the associated martensitic phase transformation [41]. From these snapshots we can determine the orientation relationships at the coherent terrace planes. The mobile interface has the following relationship (Figure 7b):

$$\begin{aligned}\left(\bar{1}12\right)_{B2} \,//\, \left(\bar{1}01\right)_{B19'}\\ [110]_{B2} \,//\, [010]_{B19'}\\ \left[1\bar{1}1\right]_{B2} \,//\, [101]_{B19'}\end{aligned}$$

We refer to this as interface 1. For the retained austenite interface, the relationship is (Figure 7c):

$$\begin{aligned}\left(\bar{1}10\right)_{B2} \,//\, (100)_{B19'}\\ [110]_{B2} \,//\, [010]_{B19'}\\ [001]_{B2} \,//\, [001]_{B19'}\end{aligned}$$

which we refer to as interface 2. Interface 2 has been proposed previously [42, 43], but interface 1 has not been reported before to the best of our knowledge. The terrace planes of each interface have an associated bi-axial coherency strain, which can be expressed as a function of the B2 lattice parameter (a_0) and the B19' lattice parameters (a, b, c, β) depending upon the orientation relationship. Parallel to the disconnection lines, which we define as the y-axis in the terrace plane reference frame, it is the same for both interfaces:

$$\epsilon_{yy} = \frac{\sqrt{2}a_0 - b}{\left(\sqrt{2}a_0 + b\right)/2} \tag{3}$$

Evaluating this expression with the relevant lattice parameters depicted in Table II gives a coherency strain of 0.22%. Typically the coherency strain parallel to the disconnection lines would be accommodated by an array of twin boundaries [41]. In our simulations however, formation of twins was suppressed due to the spring forces locking in a single martensite variant, so therefore the interfaces are fully coherent parallel to the disconnection lines. Perpendicular to the disconnection lines, which we define as the x-axis in the terrace plane reference frame, the coherency strain is different for the two interfaces. In interface 1 it can be expressed as:

$$\epsilon_{xx} = \frac{\sqrt{3}a_0 - \sqrt{a^2 + c^2 + 2ac\cos\beta}}{\left(\sqrt{3}a_0 + \sqrt{a^2 + c^2 + 2ac\cos\beta}\right)/2} \tag{4}$$

and in interface 2 as:

$$\epsilon_{xx} = \frac{a_0 - c}{\left(a_0 + c\right)/2} \tag{5}$$

For interface 1 this coherency strain is 0.33%, and for interface 2 it is 1.28%, which is accommodated by the regular arrays of disconnections. The significantly larger coherency strain present in interface 2 provides a likely reason as to why interface 1 formed preferentially in our MD simulations. We note that the coherency strains are a direct result of the lattice parameters of the two phases, suggesting that the specifics of the interatomic potential could change which interfaces are more favorable. However, using the accepted experimental lattice parameters

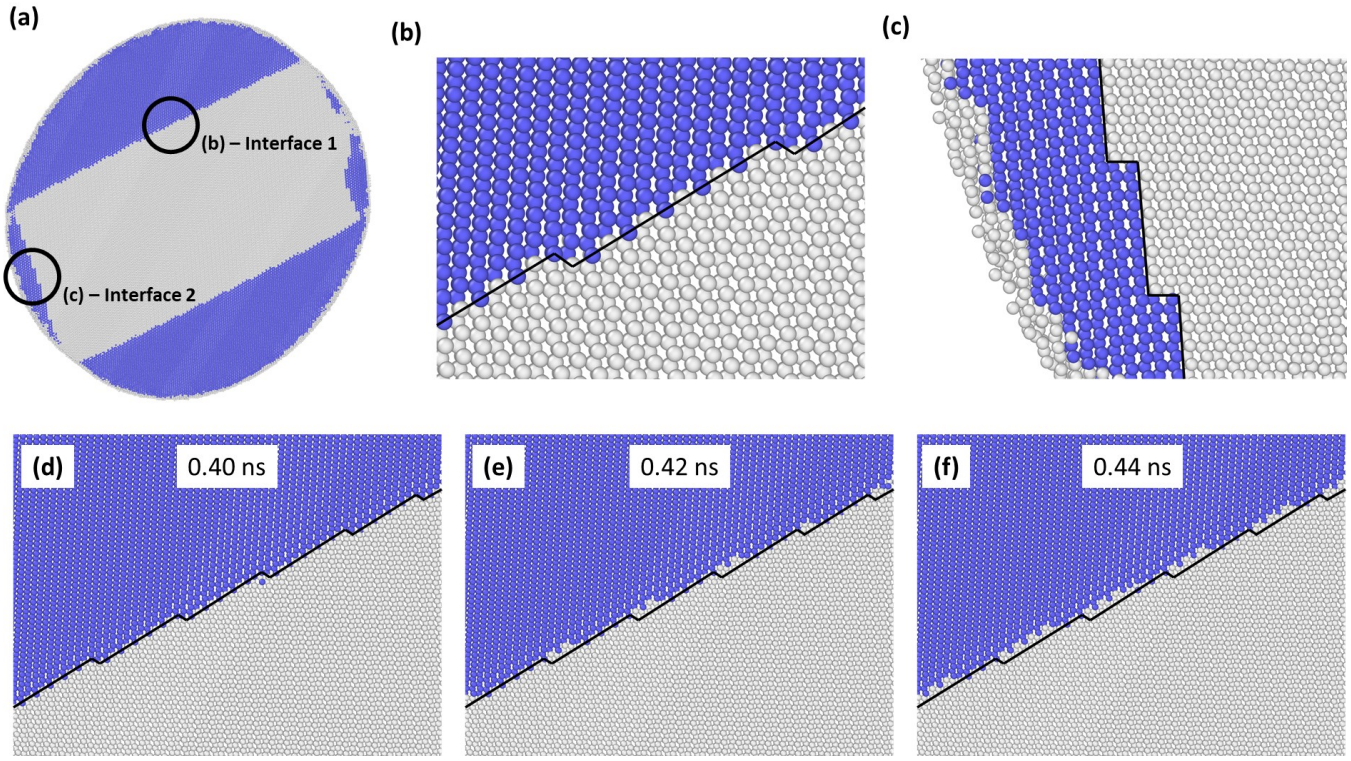

FIG. 7. (a) Snapshot of the growing B19' plate at 415 K with atomic positions averaged over 1,000 timesteps. The interfaces are made up of disconnection arrays. (b,c) Magnified images of interfaces 1 (b) and 2 (c). (d-f) Successive snapshots show the migration of interface 1 via the advancement of disconnections. The black line of the initial interface structure (d) is superimposed on all three images to emphasize the motion of the disconnections via the addition of new B19' atoms. Atoms are colored according to CNA: B2 - blue, other - gray.

[44] produces the same qualitative result, with interface 1 exhibiting significantly less coherency strain.

The structural disconnections play a prominent role in the migration of the austenite-martensite interfaces. We explore their role in the case of interface 1 by comparing a series of position-averaged snapshots from the NVT simulation at 415 K (Figure 7d-f, see also Movies S3 and S4 [35]). The disconnections act as preferential sites for new atoms to be added to the growing B19' phase, and their collective advancement leads to growth of the B19' plate. The snapshots in Figure 7, however, only give a one dimensional picture of the disconnections, which are line defects existing within the two dimensional habit plane, much as dislocations exist within a slip plane. A top-down view of the interface, which is shown in Figure 8, provides a more complete picture of their structure. The disconnections are not simply straight line defects but have numerous kinks along their length, which make them curve as they traverse the habit plane. It is these kinks which allow the disconnections to advance in a way analogous to the terrace-ledge-kink model of crystal growth [45] (Movies S5 and S6 [35]). New atoms preferentially attach to the kinks in the disconnections as this provides them with a greater number of nearest neighbors in the growing B19' phase as opposed to if they attached at a flat portion of the disconnection.

TABLE II. Lattice parameters of the B2 (a_0) and B19' phases as determined by the MEAM potential at 420 K. All distances are in Angstroms and angles in degrees.

a_0	a	b	c	β
3.01	4.58	4.22	2.86	95.9°

As the kinks move outward toward the nanoparticle surfaces due to the continuous addition of new atoms, the disconnection progressively advances forward by a single row of atoms, the exact process depicted in the side-on view of Figure 7. This is the same process as the kink pair mechanism of motion associated with dislocations in some materials [46].

Further description of the structural disconnections associated with austenite-martensite interfaces can provide additional insights into their migration. To do this we make use of the construction developed by Hirth and Pond [39], which is depicted in Figure 9. Each phase making up the interface has an associated step vector ($\mathbf{l}$). Because the phases have different lattice parameters (Table II), summation of the step vectors results in a nonzero vector associated with the gap between the crystals in Figure 9. This is defined as the Burgers vector

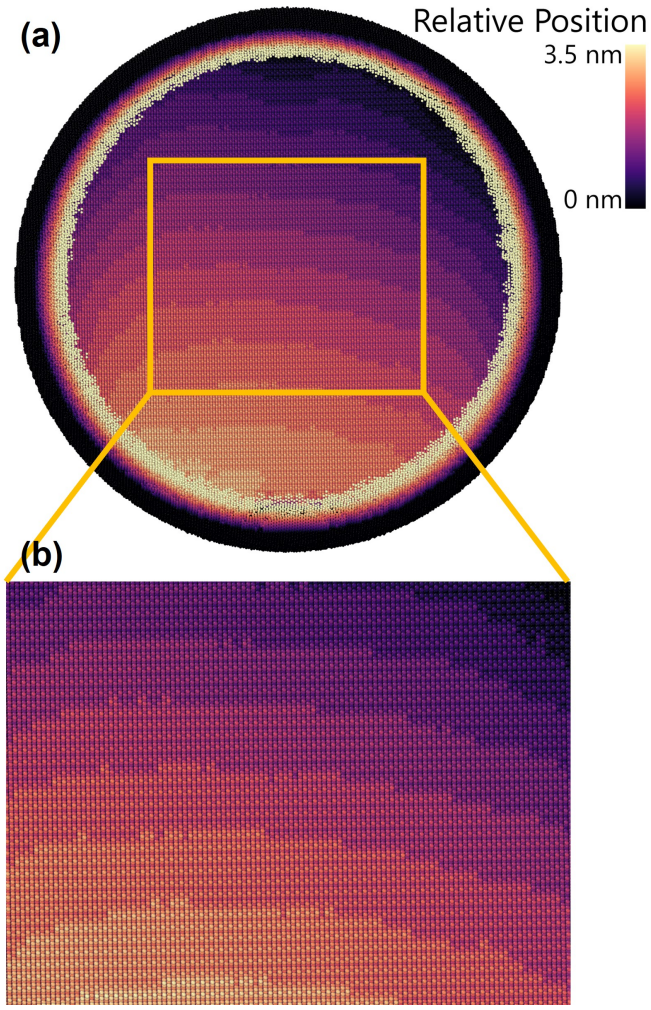

FIG. 8. Top-down view of the austenite-martensite interface showing the array of disconnections as well as a number of kinks which facilitate their motion. B2 atoms have been removed for clarity, and the remaining atoms are colored according to their position along the habit plane normal, enabling the interfacial steps to be visualized. The bright and dark rings on the perimeter correspond to surface atoms and can be disregarded.

of the disconnection ($\mathbf{b_D}$); note that in the real interface this gap is closed by interatomic interactions (Figures 7b and c). The step vectors in interfaces 1 and 2 can be determined by inspecting Figures 7b and c. For interface 1, expressed in the reference frames of their parent lattices, they are:

$$\mathbf{l_{B2}} = \frac{1}{2}\left[1\bar{1}\bar{1}\right]_{B2} \quad \text{and} \quad \mathbf{l_{B19'}} = \frac{1}{2}\left[\bar{1}01\right]_{B19'}$$

and for interface 2:

$$\mathbf{l_{B2}} = \left[\bar{1}10\right]_{B2} \quad \text{and} \quad \mathbf{l_{B19'}} = \left[100\right]_{B19'}$$

The step vectors must be transformed to a common reference frame to determine the disconnection Burgers vector. Using the appropriate lattice parameters (Table II)

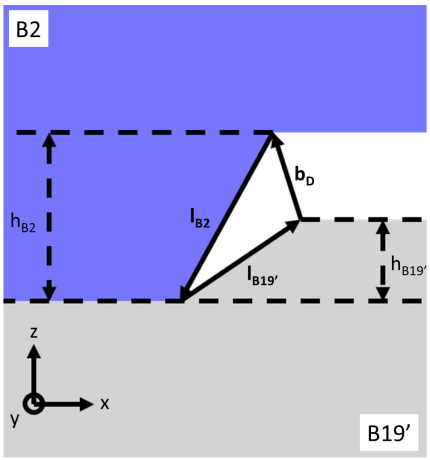

FIG. 9. Schematic of the formation of a disconnection in NiTi, when two crystals of B2 and B19' with opposite step directions are joined together. Each crystal has an associated step vector ($\mathbf{l}$) and step height (h). Summation of the two step vectors leads to the Burgers vector of the disconnection ($\mathbf{b_D}$).

TABLE III. Characteristics of the disconnections in interfaces 1 and 2 expressed in the terrace plane reference frame (Figure 9). Included are the coherency strains, step vectors, Burgers vector, Burgers vector magnitude, and angle of the Burgers vector with the terrace plane normal. All distances are in Angstroms and angles in degrees.

	Interface 1	Interface 2
ϵ_{xx}	0.33%	1.28%
ϵ_{yy}	0.22%	0.22%
$\mathbf{l_{B2}}$	$[0.87, 0, -2.463]$	$[0, 0, -4.26]$
$\mathbf{l_{B19'}}$	$[-1.24, 0, 2.53]$	$[-0.47, 0, 4.56]$
$\mathbf{b_D}$	$[-0.37, 0, 0.08]$	$[-0.47, 0, 0.30]$
$\lvert\mathbf{b_D}\rvert$	0.38	0.56
θ	78.7°	57.6°

and orientation relationships of the interfaces, the step vectors can be expressed in the reference frame of the terrace plane (see coordinate tripod in Figure 9), thus allowing for direct comparison. The resulting vectors for interfaces 1 and 2 are presented in Table III along with the Burgers vector magnitude and orientation relative to the terrace plane. Notably, the disconnections of interface 1 have a Burgers vector which is both smaller in magnitude and closer to being parallel with the terrace plane. These characteristics suggest the disconnections in interface 1 should be more energetically favorable and mobile than those in interface 2 [39], thus providing more evidence as to why interface 1 formed preferentially in our MD simulations. We leave a more detailed comparison of these two interfaces to future work, as the current nanoparticle simulations can only capture the migration of interface 1. Identification of the relevant orientation relationships should facilitate additional characterization.

V. CONCLUSIONS

Hysteresis, a prominent feature of the martensitic transformation in SMAs, is closely tied to the structure of austenite-martensite interfaces. MD simulations provide a unique opportunity to study these interfaces in detail not achievable by experiments and beyond the current capabilities of *ab initio* modeling techniques. Herein, we have developed a new method for creating well-defined austenite-martensite interfaces and have used it to study their mobility and structure in equiatomic NiTi. Critically, this new approach bypasses the extreme rates typically associated with MD simulations, which do not allow well-defined interfaces to form prior to thermodynamic instability. In well-equilibrated simulations of the coexisting phases, the martensite naturally adopts a plate morphology within the austenite matrix. This is consistent with experimental observations and indicates there are certain energetically preferred interfaces in NiTi. Application of a thermodynamic driving force to the equilibrated interfaces results in migration at velocities comparable to the time scales of experimental observations. Due to the nanoparticle geometry of the simulations, no thermal hysteresis was observed. However, changing the initial shape of the nucleus resulted in an estimated hysteresis of about 20 K solely due to the energy associated with the austenite-martensite interface. This is in much better alignment with experiments on bulk samples of NiTi rather than the results of typical rate-dependent MD simulations. While not a direct analog to experiments, our simulations directly demonstrate the important contribution of austenite-martensite interfaces to thermal hysteresis in SMAs.

Additional analysis of the austenite-martensite interfaces revealed that they are made up of coherent terrace planes separated from one another by structural disconnections. Identification of the orientation relationships at the terrace planes as well as characteristics of the disconnections provides evidence as to why certain interfaces are energetically preferred in NiTi. The disconnections provide an atomic-scale mechanism for interface migration, as new atoms preferentially attach at kinks along their length in a manner analogous to the terrace-ledge-kink model of crystal growth. The continual advancement of a train of disconnections leads to the overall migration of the interface. Overall, the methodology presented here should serve as an important step toward better utilizing MD simulations to understand the martensitic transformation in SMAs. The specific results in NiTi provide interesting directions for the further study of austenite-martensite interfaces and their contribution to hysteresis.

ACKNOWLEDGMENTS

Funding is acknowledged from the NASA Aeronautics Research Mission Directorate's (ARMD) Transformational Tools and Technologies (TTT) Project. We benefited from discussions with Othmane Benafan and Santo Padula. Resources supporting this work were provided by the NASA High-End Computing (HEC) Program through the NASA Advanced Supercomputing (NAS) Division at Ames Research Center.

[1] J. M. Jani, M. Leary, A. Subic, and M. A. Gibson, A review of shape memory alloy research, applications and opportunities, Materials & Design **56**, 1078 (2014).

[2] K. Otsuka and X. Ren, Physical metallurgy of Ti–Ni-based shape memory alloys, Progress in Materials Science **50**, 511 (2005).

[3] H. Gu, L. Bumke, C. Chluba, E. Quandt, and R. D. James, Phase engineering and supercompatibility of shape memory alloys, Materials Today **21**, 265 (2018).

[4] J. Frenzel, E. P. George, A. Dlouhy, C. Somsen, M. F.-X. Wagner, and G. Eggeler, Influence of Ni on martensitic phase transformations in NiTi shape memory alloys, Acta Materialia **58**, 3444 (2010).

[5] Z. Zhang, R. D. James, and S. Müller, Energy barriers and hysteresis in martensitic phase transformations, Acta Materialia **57**, 4332 (2009).

[6] Y. Song, X. Chen, V. Dabade, T. W. Shield, and R. D. James, Enhanced reversibility and unusual microstructure of a phase-transforming material, Nature **502**, 85 (2013).

[7] C. Chluba, W. Ge, R. Lima de Miranda, J. Strobel, L. Kienle, E. Quandt, and M. Wuttig, Ultralow-fatigue shape memory alloy films, Science **348**, 1004 (2015).

[8] R. Sinclair and H. A. Mohamed, Lattice imaging study of a martensite-austenite interface, Acta Metallurgica **26**, 623 (1978).

[9] G. J. Mahon, J. M. Howe, and S. Mahajan, HRTEM study of the $\{252\}_\gamma$ austenite–martensite interface in an Fe—8Cr–1C alloy, Philosophical Magazine Letters **59**, 273 (1989).

[10] Y. W. Chai, H. Y. Kim, H. Hosoda, and S. Miyazaki, Interfacial defects in Ti–Nb shape memory alloys, Acta Materialia **56**, 3088 (2008).

[11] R. Delville, S. Kasinathan, Z. Zhang, J. V. Humbeeck, R. D. James, and D. Schryvers, Transmission electron microscopy study of phase compatibility in low hysteresis shape memory alloys, Philosophical Magazine **90**, 177 (2010).

[12] Y. Zhong, K. Gall, and T. Zhu, Atomistic study of nanotwins in NiTi shape memory alloys, Journal of Applied Physics **110**, 033532 (2011).

[13] W.-S. Ko, B. Grabowski, and J. Neugebauer, Development and application of a Ni-Ti interatomic potential with high predictive accuracy of the martensitic phase transition, Physical Review B **92**, 134107 (2015).

[14] G. Ren and H. Sehitoglu, Interatomic potential for the

NiTi alloy and its application, Computational Materials Science **123**, 19 (2016).
[15] H. Tang, Y. Zhang, Q.-J. Li, H. Xu, Y. Wang, Y. Wang, and J. Li, High accuracy neural network interatomic potential for NiTi shape memory alloy, Acta Materialia **238**, 118217 (2022).
[16] Y. Zhong, K. Gall, and T. Zhu, Atomistic characterization of pseudoelasticity and shape memory in NiTi nanopillars, Acta Materialia **60**, 6301 (2012).
[17] R. Mirzaeifar, K. Gall, T. Zhu, A. Yavari, and R. DesRoches, Structural transformations in NiTi shape memory alloy nanowires, Journal of Applied Physics **115**, 194307 (2014).
[18] W.-S. Ko, S. B. Maisel, B. Grabowski, J. B. Jeon, and J. Neugebauer, Atomic scale processes of phase transformations in nanocrystalline NiTi shape-memory alloys, Acta Materialia **123**, 90 (2017).
[19] W.-S. Ko, B. Grabowski, and J. Neugebauer, Impact of asymmetric martensite and austenite nucleation and growth behavior on the phase stability and hysteresis of freestanding shape-memory nanoparticles, Physical Review Materials **2**, 030601(R) (2018).
[20] A. P. Thompson, H. M. Aktulga, R. Berger, D. S. Bolintineanu, W. M. Brown, P. S. Crozier, P. J. in't Veld, A. Kohlmeyer, S. G. Moore, T. D. Nguyen, R. Shan, M. J. Stevens, J. Tranchida, C. Trott, and S. J. Plimpton, LAMMPS-a flexible simulation tool for particle-based materials modeling at the atomic, meso, and continuum scales, Computer Physics Communications **271**, 108171 (2022).
[21] A. Stukowski, Visualization and analysis of atomistic simulation data with OVITO–the open visualization tool, Modelling and Simulation in Materials Science and Engineering **18**, 015012 (2009).
[22] D. Faken and H. Jónsson, Systematic analysis of local atomic structure combined with 3D computer graphics, Computational Materials Science **2**, 279 (1994).
[23] R. Freitas, M. Asta, and M. De Koning, Nonequilibrium free-energy calculation of solids using LAMMPS, Computational Materials Science **112**, 333 (2016).
[24] V. V. Shastry, V. D. Divya, M. A. Azeem, A. Paul, D. Dye, and U. Ramamurty, Combining indentation and diffusion couple techniques for combinatorial discovery of high temperature shape memory alloys, Acta Materialia **61**, 5735 (2013).
[25] R. R. Pezarini, H. S. Bernabé, F. Sato, L. C. Malacarne, N. G. C. Astrath, J. H. Rohling, A. N. Medina, R. D. Dos Reis, and F. C. G. Gandra, On the use of photothermal techniques to study NiTi phase transitions, Materials Research Express **1**, 026502 (2014).
[26] J. B. Haskins, A. E. Thompson, and J. W. Lawson, *Ab initio* simulations of phase stability and martensitic transitions in NiTi, Physical Review B **94**, 214110 (2016).
[27] J. B. Haskins and J. W. Lawson, Finite temperature properties of NiTi from first principles simulations: Structure, mechanics, and thermodynamics, Journal of Applied Physics **121**, 205103 (2017).
[28] J. B. Haskins, H. Malmir, S. J. Honrao, L. A. Sandoval, and J. W. Lawson, Low-temperature mechanical instabilities govern high-temperature thermodynamics in the austenite phase of shape memory alloy constituents: *Ab Initio* simulations of NiTi, NiZr, NiHf, PdTi, and PtTi, Acta Materialia **212**, 116872 (2021).
[29] Z. Wu and J. W. Lawson, Theoretical investigation of phase transitions in the shape memory alloy NiTi, Physical Review B **106**, L140102 (2022).
[30] D. Dickel, C. D. Barrett, R. L. Carino, M. I. Baskes, and M. F. Horstemeyer, Mechanical instabilities in the modeling of phase transitions of titanium, Modelling and Simulation in Materials Science and Engineering **26**, 065002 (2018).
[31] R. J. Wasilewski, S. R. Butler, and J. E. Hanlon, On the martensitic transformation in TiNi, Metal Science Journal **1**, 104 (1967).
[32] W. Tang, B. Sundman, R. Sandström, and C. Qiu, New modelling of the B2 phase and its associated martensitic transformation in the Ti–Ni system, Acta Materialia **47**, 3457 (1999).
[33] J. R. Morris, C. Z. Wang, K. M. Ho, and C. T. Chan, Melting line of aluminum from simulations of coexisting phases, Physical Review B **49**, 3109 (1994).
[34] S. Yoo, X. C. Zeng, and J. R. Morris, The melting lines of model silicon calculated from coexisting solid–liquid phases, The Journal of Chemical Physics **120**, 1654 (2004).
[35] See supplemental material at (url) for additional simulation data and movies.
[36] J. Michutta, C. Somsen, A. Yawny, A. Dlouhy, and G. Eggeler, Elementary martensitic transformation processes in Ni-rich NiTi single crystals with Ni_4Ti_3 precipitates, Acta Materialia **54**, 3525 (2006).
[37] T. Simon, A. Kröger, C. Somsen, A. Dlouhy, and G. Eggeler, On the multiplication of dislocations during martensitic transformations in NiTi shape memory alloys, Acta Materialia **58**, 1850 (2010).
[38] J. P. Hirth, Dislocations, steps and disconnections at interfaces, Journal of Physics and Chemistry of Solids **55**, 985 (1994).
[39] J. P. Hirth and R. C. Pond, Steps, dislocations and disconnections as interface defects relating to structure and phase transformations, Acta Materialia **44**, 4749 (1996).
[40] J. M. Howe, R. C. Pond, and J. P. Hirth, The role of disconnections in phase transformations, Progress in Materials Science **54**, 792 (2009).
[41] R. C. Pond, S. Celotto, and J. P. Hirth, A comparison of the phenomenological theory of martensitic transformations with a model based on interfacial defects, Acta Materialia **51**, 5385 (2003).
[42] R. C. Pond and T. Nixon, Nucleation and growth in martensitic transformations, MRS Online Proceedings Library **580**, 303 (1999).
[43] S. Alkan and H. Sehitoglu, Prediction of transformation stresses in NiTi shape memory alloy, Acta Materialia **175**, 182 (2019).
[44] S. D. Prokoshkin, A. V. Korotitskiy, V. Brailovski, S. Turenne, I. Y. Khmelevskaya, and I. B. Trubitsyna, On the lattice parameters of phases in binary Ti–Ni shape memory alloys, Acta Materialia **52**, 4479 (2004).
[45] W. K. Burton, N. Cabrera, and F. C. Frank, The growth of crystals and the equilibrium structure of their surfaces, Philosophical Transactions of the Royal Society of London. Series A, Mathematical and Physical Sciences **243**, 299 (1951).
[46] P. M. Anderson, J. P. Hirth, and J. Lothe, *Theory of dislocations* (Cambridge University Press, 2017).